Journal of Alloys and Compounds 509 (2011) 6924–6929

Contents lists available at ScienceDirect

Journal of Alloys and Compounds

journal homepage: www.elsevier.com/locate/jallcom

Epitaxial PMN–PT thin films grown on buffered Si substrates using ceramic and single-crystal targets

Juan Jiang[a], Hyun-June Jung[a], Soon-Gil Yoon[a,b,*]

[a] School of Nano Science and Technology Chungnam National University, Daeduk Science Town, Daejeon 305-764, Republic of Korea
[b] Graduate of Analytical Science and Technology (GRAST), Chungnam National University, Daeduk Science Town, Daejeon 305-764, Republic of Korea

ARTICLE INFO

Article history:
Received 21 November 2010
Received in revised form 30 March 2011
Accepted 1 April 2011
Available online 7 April 2011

Keywords:
Epitaxial PMN–PT thin films
Electrical properties
Pulse laser deposition
Single crystal target
Ceramics target

ABSTRACT

Epitaxial $0.65Pb(Mg_{1/3}Nb_{2/3})O_3$–$0.35PbTiO_3$ (PMN–PT) thin films were deposited on LSCO/CeO_2/YSZ tri-buffered Si substrate by pulsed laser deposition (PLD) using sintered ceramic and single-crystal targets. The PMN–PT films deposited using both targets were single crystalline and exhibited cube-on-cube growth epitaxy with the substrate. The films deposited using the single-crystal target showed higher crystallinity and a smoother surface morphology than those grown using the ceramic target. The crystallinity of films can be affected by the in-plane lattice mismatch of PMN–PT/LSCO interfaces. The low density and low absorption coefficient of the sintered ceramic target were responsible for the severe compositional deviation from the desired stoichiometry of the PMN–PT films. Dielectric constants of approximately 1926 and 1540 at 10 kHz were obtained for the films deposited using the single-crystal and sintered ceramic target, respectively. In addition, the PMN–PT films fabricated using the single-crystal target exhibited well-developed polarization hysteresis loops with a remnant polarization of 11.9 $\mu C/cm^2$. Single-crystal targets are an indispensable candidate for the growth of epitaxial PMN–PT films with high crystallinity and good electrical properties.

1. Introduction

Due to high dielectric permittivity and piezoelectric properties, lead magnesium niobate $Pb(Mg_{1/3}Nb_{2/3})O_3$ (PMN) and its solid solution with $PbTiO_3$ (PT), in both bulk and thin film forms, are potentially promising candidates for various microelectromechanical systems (MEMS) [1]. A combination of 65 at.% of PMN with 35 at.% of PT is known as the morphotropic phase boundary (MPB), which separates the tetragonal and rhombohedral perovskite phases of $0.65Pb(Mg_{1/3}Nb_{2/3})O_3$–$0.35PbTiO_3$ (PMN–PT). The interest in PMN–PT thin films results from the growing need for miniaturized electromechanical actuators, transducers, and sensors in various fields of science and technology. However, PMN–PT films on noble metal electrodes like Pt exhibit significant fatigue after the long bipolar switching pulses used in memory application. To overcome this fatigue problem in PMN–PT, metallic oxide electrodes such as $La_{0.5}Sr_{0.5}CoO_3$ (LSCO) [2], $SrRuO_3$ (SRO) [3], and $LaNiO_3$ (LNO) [4], replacing the noble metal electrodes like Pt [5], are thought to be one possible solution.

Epitaxial films are expected to exhibit improved properties compared to their randomly oriented polycrystalline film counterparts. Although researchers have already obtained good epitaxial PMN–PT thin films on some single crystal substrates such as $SrTiO_3$ [6], Al_2O_3 [7], and $LaAlO_3$ [8] using different deposition methods (sputtering, pulsed laser deposition, and metal-organic chemical-vapor deposition), fabrication on silicon is preferred for industrial applications, because it is a much cheaper substrate and also provides the promise that it can be integrated with a complementary metal-oxide semiconductor process. In order to grow epitaxial PMN–PT thin films on an Si substrate, suitable buffer layers with good diffusion barrier properties and Si epitaxy must be used. LSCO is an example of a metallic oxide with a cubic perovskite structure. The resistivity at 300 K is approximately 2,300 $\mu\Omega$ cm, which makes LSCO a favorable electrode candidate for ferroelectric thin films.

The major challenge of thin film processing is the deposition of pyrochlore-free PMN–PT. Pulse laser deposition (PLD) is a powerful technique for stoichiometric transfer from a multicomponent oxide target to a growing film. For PMN–PT targets, both ceramic and single-crystal forms can be used. Since the single-crystal form exhibits higher thermal conductivity and a perfect structure, the surface can homogeneously absorb the incident laser energy. Compared with ceramics, single-crystal PMN–PTs continue to exhibit better electrical properties [9]. However, few systematic reports

---

* Corresponding author at: School of Nano Science and Technology Chungnam National University, Daeduk Science Town, Daejeon 305-764, Republic of Korea. Tel.: +82 42 821 6638; fax: +82 42 822 3206.
E-mail address: sgyoon@cnu.ac.kr (S.-G. Yoon).

0925-8388/$ – see front matter. Crown Copyright © 2011 Published by Elsevier B.V. All rights reserved.
doi:10.1016/j.jallcom.2011.04.002

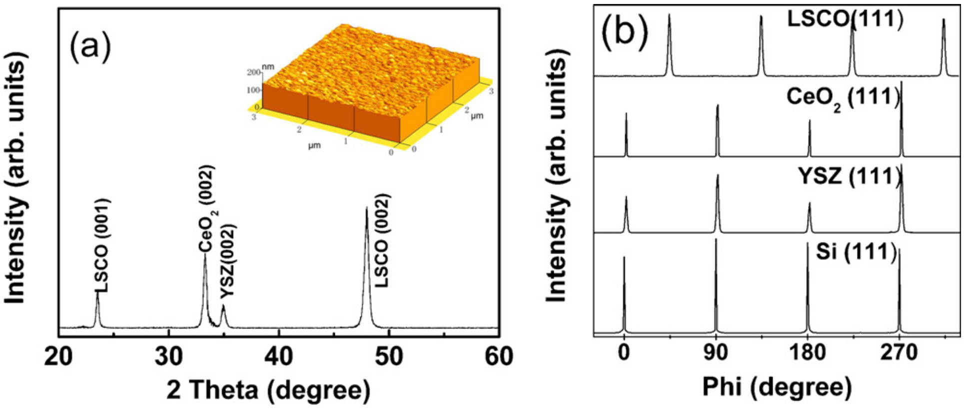

Fig. 1. (a) XRD θ–2θ pattern of a typical LSCO bottom electrode deposited on CeO$_2$/YSZ/Si (0 0 1) and (b) phi-scans measured at (1 1 1) reflection of each layer. The inset in (a) shows the three-dimensional AFM image of the LSCO film grown on CeO$_2$/YSZ/Si substrate.

Table 1
Deposition conditions of PMN–PT, LSCO, CeO$_2$, and YSZ films onto Si substrates.

Deposition parameters	YSZ	CeO$_2$	LSCO	PMN–PT
Deposition temperature (°C)	750	750	550	550
Film thickness (nm)	70	35	90	500
Deposition pressure (mTorr)	0.5	0.5	300	300
Energy density (J/cm^2)	1.5	1.5	1.5	1.5
Target–substrate distance(cm)	8	8	6	6

have compared the structures and electrical properties of films deposited using different targets. As far as can be ascertained, this is the first report of the effect of different targets on the composition, crystallinity, morphology, and electrical properties of PMN–PT films. In the present study, 500-nm-thick PMN–PT epitaxial thin films were grown by PLD on a LSCO/CeO$_2$/YSZ trilayer buffered Si (0 0 1) substrate at 550 °C using a single-crystal and a ceramic target. The effect of the target forms on the properties of PMN–PT films was systematically investigated in the present study.

2. Experimental

500-nm-thick 0.65PMN-0.35PT films were fabricated using the PLD technique with a 248 nm KrF excimer laser from a sintered ceramic and a single-crystal target. The laser beam hit the target at an incident angle of 45°. The substrate was placed parallel to the target. The YSZ, CeO$_2$, and LSCO targets used in the present study were prepared by standard solid-state reactions of the constituent oxides. The 0.65PMN–0.35PT ceramic target was fabricated by first processing stoichiometric PMN–PT powder at the desired 65/35 ratio, followed by the columbite method. A 10 wt.% excess of PbO was added to the PMN–PT powder to compensate for the loss of PbO during sintering, and the powders were ball-milled in ethanol for 4 h to insure homogeneous distribution. Pellets with a diameter of 1 inch were uniaxially pressed without binder. The samples were sintered at 950 °C in ambient air for 1 h, and their density was approximately 90%. The 0.65PMN–0.35PT single-crystal target, above 98% density, was provided by a Korean crystal manufacturer, IBULE Photonics, Inc. (www.ibule.com).

The deposition conditions of the PMN–PT/LSCO/CeO$_2$/YSZ heterostructure onto Si (0 0 1) substrates are summarized in Table 1. PMN–PT films using both the ceramic and single-crystal target were deposited at a substrate temperature of 550 °C at an oxygen pressure of 30 mTorr. After deposition, high-purity oxygen (99.99%) was introduced into the growth chamber to maintain 600 Torr pressure, and the as-prepared films were maintained at the same temperature for 10 min and then cooled naturally to room temperature.

The film thicknesses were measured through cross-sectional scanning electron microscopy (SEM) images. The surface morphologies of the PMN–PT films and the buffer layers were measured by atomic force microscopy (AFM, AUTOPROBE CP, PSI). The phase, crystallinity, and epitaxial relationship of the heterostructure were investigated by θ–2θ, ω-scan and Φ-scan, respectively, using high-resolution X-ray diffraction (HRXRD, Rigaku RINT2000). The resistivity of the LSCO thin films was measured by an electrometer (CMT-SR 1000) using a four-point probe. The composition of each element in the PMN–PT films was determined by Electron Probe Micro-analysis (EPMA). The elemental distribution in the PMN–PT/LSCO/CeO$_2$/YSZ/Si structure was investigated using secondary ion mass spectroscopy (SIMS). The microstructure and the interface of the films were studied using high-resolution transmission electron microscopy (TEM: JEM-2100F).

To measure the electrical properties of the PMN–PT films, conventional photolithography was used to pattern the Pt top electrodes of 100 µm diameter deposited by direct-current sputtering. The polarization vs. electric field (*P*–*E*) curve of the films was measured using a RT66A ferroelectric tester (Radiant Technology) operating in the virtual ground mode. The dielectric constant and losses were obtained by impedance analysis with a HP4194A apparatus with a frequency that ranged from 100 Hz to 1 MHz.

3. Results and discussion

The XRD θ–2θ pattern of a typical LSCO bottom electrode deposited on CeO$_2$/YSZ/Si (0 0 1) at an optimized temperature of 550 °C and an oxygen pressure of 300 mTorr is shown in Fig. 1(a). The peaks corresponding to the (0 0 1) reflections of the heterostructure were observed with no other minor peaks. The full-width at half-maximum (FWHM) of the rocking curves for the LSCO (0 0 2) peaks (not shown here) was about 1.29°. The inset in Fig. 1(a) shows the three-dimensional AFM images of the LSCO films grown on a CeO$_2$/YSZ/Si substrate. No cracks or laser-induced droplets were observed on the surface of the LSCO films. The 90-nm- thick LSCO films showed an extremely smooth structure with a root mean square (rms) roughness of about 1.9 nm, a promising property for the subsequent growth of highly oriented ferroelectric thin films. Resistivity of the epitaxial LSCO films was approximately 2100 µΩ cm. The epitaxial relationship was confirmed by means of phi-scans measured at (1 1 1) reflection of each layer

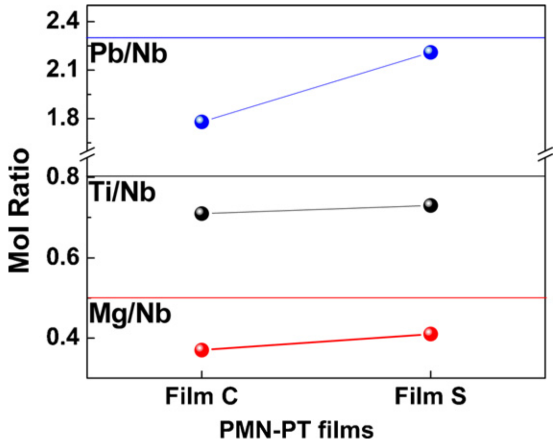

Fig. 2. Elemental compositions of films S and C. The horizontal lines show the elemental composition of each PMN–PT target.

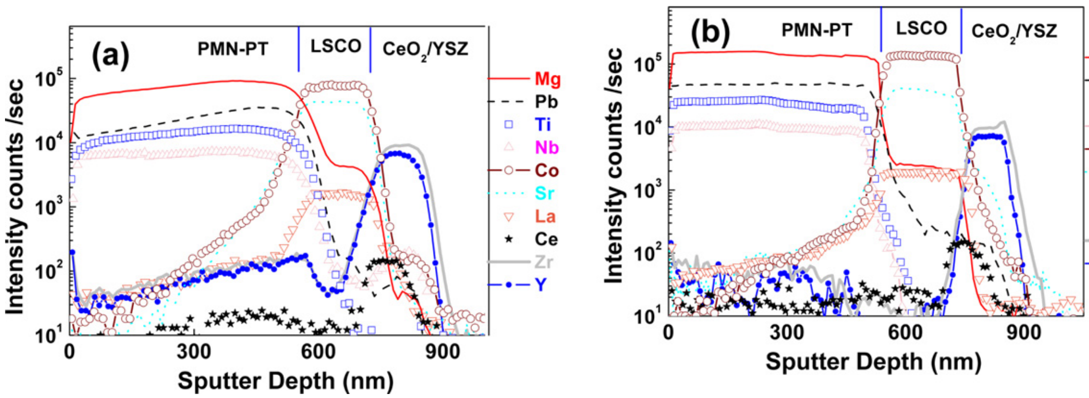

Fig. 3. Elemental distribution in each layer of (a) film C and (b) film S.

(Fig. 1(b)). The 4-fold symmetry peaks revealed that the epitaxial relationship between the 3 different layers and the substrate was: (0 0 1)[1 1 0]LSCO//(0 0 1)[1 0 0]CeO_2//(0 0 1)[1 0 0]YSZ//(0 0 1)[1 0 0]Si. The 45° in-plane relationship was attributed to the low mismatch between the diagonal of a face of the LSCO pseudocubic unit cell and the CeO_2 lattice parameter.

The compositions of the PMN–PT films are represented in terms of the cation ratios of Pb/Nb, Mg/Nb and Ti/Nb, as shown in Fig. 2. The films deposited using the single-crystal and the ceramic target are denoted as films “S” and “C”, respectively. Compared to their initial composition in the targets (indicated as horizontal lines), a slight loss of Pb and Mg content was attributed to the volatilization of the elements by the elevated deposition temperatures of 550 °C [10], and an unexpected Ti loss was observed. Film C shows a larger deficiency of Pb and Mg than film S, although the films were deposited under identical conditions. The difference in the compositions of film S and film C may be attributed to the difference in the density of the targets used.

The elemental distribution in the epitaxial PMN–PT films grown using the ceramic and single-crystal targets is shown in Fig. 3(a) and (b), respectively. Film S showed more homogeneous thickness profiles than the films grown using a ceramic target. The sintered ceramic target is known to have a granular structure with various degrees of porosity (meaning a relatively lower density) and a lower thermal conductivity than the single-crystal target. When the incident laser beam was applied to the porous sintered target, off-stoichiometric evaporation occurred due to anisotropic absorption of the incident laser beam [10]. During laser ablation for a long period, both the deposition rate and the visible plume length decreased to smaller values in the case of the ceramic target. This could be the reason for severe compositional deviation from the desired stoichiometry in the case of the PMN–PT films deposited using a ceramic target. On the other hand, the single-crystal target had a large laser absorption coefficient, which resulted in maintenance of the deposition rate and the plume length.

Fig. 4(a) shows the XRD θ–2θ patterns for the as-grown film C and film S. It is clear that the orientations of the PMN–PT films are strongly correlated with those of the underlayers, and no evidence of misoriented peaks, such as (1 1 0), or of a metastable pyrochlore phase was observed. Fig. 4(b) shows the rocking curves for the PMN–PT (0 0 2) peaks of both samples. The FWHM values of film S and film C were about 1.18° and 1.25°, respectively, indicating higher crystallinity in the case of film S, which agreed well with the XRD results. To evaluate the in-plane texture, a Φ-scan of the PMN–PT (1 1 1) and LSCO (1 1 1) was also performed. As shown in the inset of Fig. 4(b), four strong peaks were observed and the average FWHM value was about 1.51° for film S and 1.75° for film C. These results suggest that film S shows better epitaxial texture than film C, and the epitaxial nature of the tri-buffered substrate was transferred well to the PMN–PT film in both cases. The crystallinity of films can also be affected by the kinetics of the species deposited on the substrate. During the laser ablation process, the kinetics of the deposited species is determined by the substrate temperature and by the energy of the atoms in the plume. Even at the same substrate temperature, due to a low absorption coefficient of the sintered ceramic target, insufficient reaction between the ambient oxygen and ions in the laser-induced plume leads to a relatively lower quality of the epitaxial PMN–PT films.

The SEM surface images of films C and S studied by SEM are shown in Fig. 5(a) and (b), respectively. Faceted shape outgrowth features were observed in both films. With the exception of the

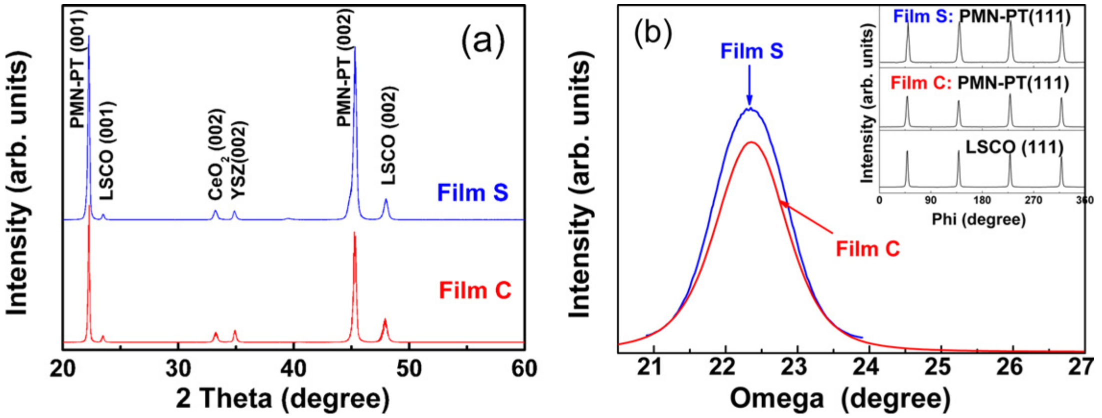

Fig. 4. (a) XRD θ–2θ patterns and (b) rocking curves for PMN–PT (0 0 2) peaks of films S and C. The inset in (b) shows Φ-scans of the PMN–PT (1 1 1) and LSCO (1 1 1).

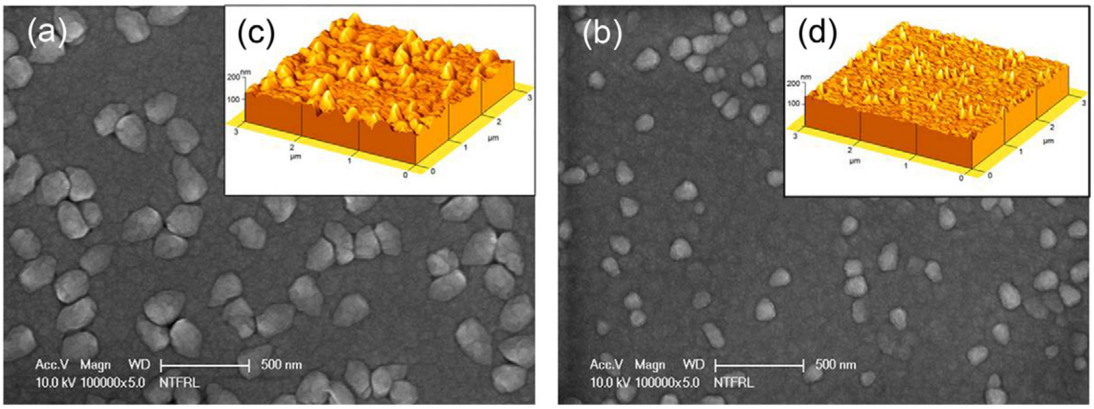

Fig. 5. SEM images of (a) film C and (b) film S. Three-dimensional AFM image of (c) film C and (d) film S.

droplets and the out-growths, the surface itself showed a very smooth and crack-free morphology. Compared with film C, film S showed a low density and small out-growths of less than 0.1 μm in base diameter. These microstructural features were similar to those previously reported for epitaxial thin films of perovskite oxides [11]. As shown in the insets of Fig. 5(c) and (d), 3-dimensional AFM images of films C and S, respectively, were taken on a 3 μm × 3 μm scale. Root-mean-square (rms) roughness of film C and S was approximately 8.9 and 6.1 nm, respectively. This result indicates that the quality of film S is better than film C.

Further study of the microstructure of the PMN–PT films was done by transmission electron microscopy (TEM), including the selected area electron diffraction (SAED) pattern. Fig. 6(a) and (b) displays the cross-sectional TEM image and SAED pattern of PMN–PT film grown using ceramic and single-crystal targets, respectively. Both of the heterostructures show a uniform dense morphology and clear interfaces between the continuous layers. Moreover, the size of the out-growth developed on top of the uniform PMN–PT layer (film C) is larger than that of film S, as determined by SEM investigations (Fig. 5). Fig. 6(c) shows a high-resolution TEM image measured at the PMN–PT/LSCO interfaces (circle part in Fig. 6(b)). Misfit dislocations and lattice deformation of PMN–PT were clearly observed in the image. The SAED patterns of the PMN–PT/LSCO interface (zone axis: [0 0 1]) and the CeO_2/YSZ interface (zone axis: [0 1 1]) are shown in Fig. 6(d) and (e), respectively. From the SAED patterns, the alignments between CeO_2/YSZ and LSCO/PMN–PT showed a 45° twisted cube-on-cube epitaxial relationship. Fig. 6(f) and (g) show the SAED images of an epitaxial PMN–PT layer in films C and S, respectively. For film C, the broad width of PMN–PT reflections [see blow-up], when compared with that of film S, was attributed to the degraded hetero-epitaxial crystalline quality of PMN–PT films, which is consistent with the FWHM values obtained from the rocking curves [Fig. 4(b)].

The dielectric properties of film C and film S were measured at room temperature using the Pt top electrode (100 μm diameter). The frequency dependences of the dielectric constant (ε_r) and the dielectric loss (tan δ) of film C and film S are shown in Fig. 7(a). In comparison with reported data [12], both the PMN–PT films possessed a relatively higher dielectric constants within the frequency range, and film S had a higher dielectric constant than film C. For film S, ε_r and tan δ were approximately 1,926 and 0.05 at 1 kHz, respectively. The enhanced crystalline quality of film S could be responsible for the improvement of the dielectric constant. No noticeable change in tan δ in either film was found in the present study below the frequency of 100 kHz. The ferroelectric behavior of the PMN–PT thin films was confirmed from the irreversible nature

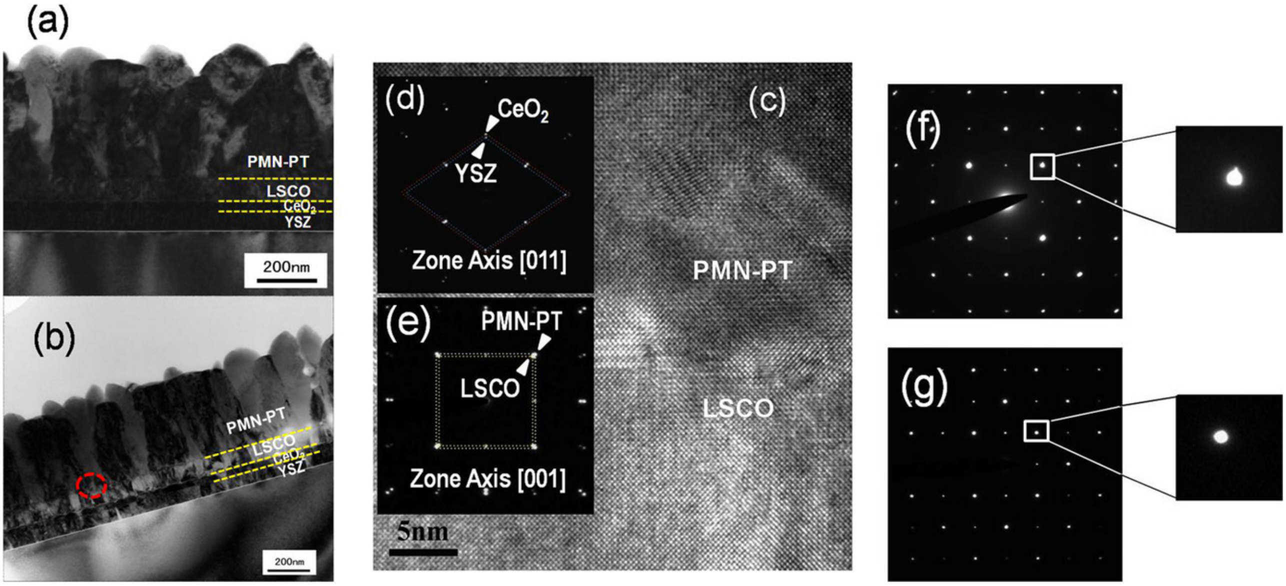

Fig. 6. Cross-sectional TEM image of the PMN–PT/LSCO/CeO_2/YSZ film grown using (a) ceramic and (b) single-crystal target. (c) High resolution TEM image of the PMN–PT/LSCO interfaces. SAED patterns of (d) CeO_2/YSZ and (e) PMN–PT/LSCO interfaces. SAED patterns of PMN–PT layers of (f) film C and (g) film S.

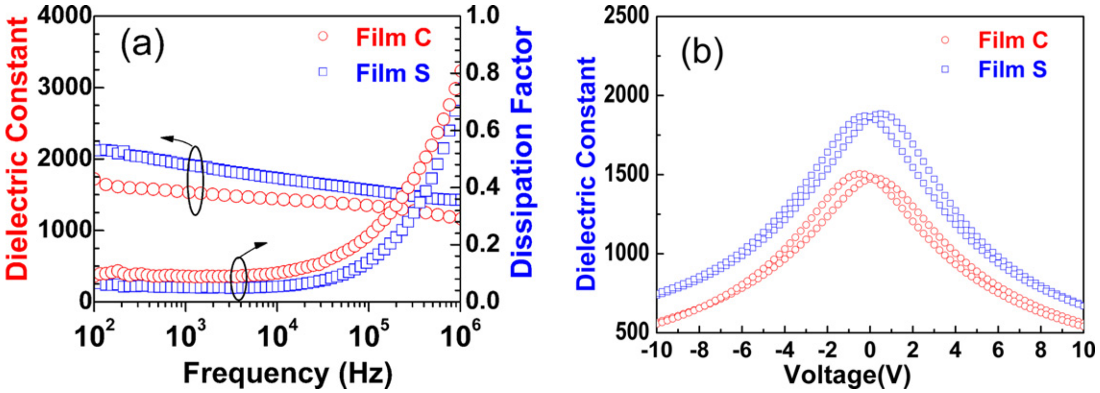

Fig. 7. (a) Frequency dependence on the dielectric constant and the dielectric loss of film S and film C and (b) dielectric constant versus voltage characteristics of film S and film C.

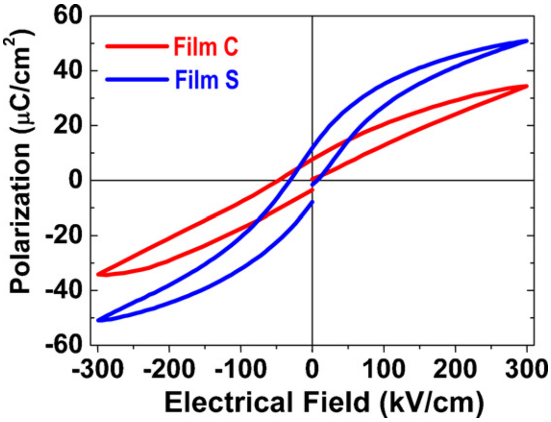

Fig. 8. Polarization–electric field (*P*–*E*) hysteresis loops for film S and film C.

of capacitance versus voltage curve. Fig. 7(b) shows the dielectric constant versus voltage (ε_r–V) characteristics for films C and film S, as measured at the frequency of 1 kHz. The results, which exhibited a butterfly shape in the ε_r–V curve, indicated that both films had a ferroelectric property. The asymmetric shape in the ε_r–V curve showed that the interfaces between the bottom and the top electrode were different. Several reasons may account for the difference in the top and bottom interfaces of the grown films, among which are the different chemical defects present at the two interfaces and the different electrode materials used for the contacts.

The polarization-electric field (*P*–*E*) hysteresis loops of epitaxial films S and C were taken at a frequency of 1 kHz. Fig. 8 shows the *P*–*E* hysteresis loop, and the remnant polarization (P_r) of films S and C was 11.9 and 7.2 μC/cm^2, respectively. The P_r values were higher than those of polycrystalline films prepared by sputtering [13] or PLD [14], and comparable to the value obtained by Chaudhuri et al. [8] for epitaxial films grown by the PLD technique.

In addition, the coercive fields of films S and C were 30.6 and 46.7 kV/cm, respectively. Crystallographic defects can pin the domain walls during the switching of the polarization, so that larger applied voltages are needed. The lattice parameters and the occurrences of a tetragonal nature (*c*/*a*) of the PMN–PT films are listed in Table 2. The lattice parameters of the bulk PMN–PT were summarized from Ref. [15]. Based on the lattice parameters of the PMN–PT bulk and LSCO films (0.381 nm from XRD), films S and C were compressed at the interface between the PMN–PT film and the buffer layer. Because of its tetragonal nature, film C experienced a higher compressive stress than film S. Based on the fact that ferroelectricity originates from crystal distortion [1], the ferroelectricity of the PMN–PT film was strongly affected by the strain energy accumulated by the lattice mismatch between the PMN–PT film and the buffer layers. As the compressive strain increased, it made movement of the domain wall difficult, resulting in the higher coercive field of film C [16,17]. Therefore, it can be concluded that a suitable choice for the target plays an important role in the improvement of the crystalline quality and the electrical properties of epitaxial films.

Table 2
Lattice parameters and tetragonality (*c*/*a*) of the bulk PMN–PT and the PMN–PT films.

PMN–PT	Lattice parameter (nm)		Tetragonality *c*/*a*
	a	*c*	
Bulk	0.400	0.404	1.010
Film S	0.391	0.400	1.023
Film C	0.387	0.403	1.041

The electrical properties mentioned above are inferior to those of the films grown on oxide single-crystal substrates [8]. One possible reason could be the presence of structural imperfections in the micro-domain of the Mg/Nb site, due to local compositional irregularities. In addition, the electrical properties of PMN–PT in the present study are inferior to those of PMN–PT sintered bodies or single crystals. This could be due to the effect of the grain size associated with the stabilization of intermediate submicrometer/nanoscale polar domain configurations [18]. Other effects, such as thermal expansion coefficient mismatch, interface layer, and size effects, may also contribute to the low dielectric and ferroelectric properties in films grown on a buffered Si substrate.

4. Conclusions

PMN–PT/LSCO/CeO$_2$/YSZ heterostructures were epitaxially grown on a Si substrate by PLD using sintered ceramic and single-crystal targets. Compared with the films deposited using the sintered ceramic target, the surface morphology and crystallinity of the films deposited using the single-crystal target were greatly improved. The crystallinity of the films was affected by the in-plane lattice mismatch of PMN–PT/LSCO interfaces and the kinetics of the species deposited on the substrate. The relatively lower density and lower absorption coefficient of the sintered ceramic target were found to be responsible for severe compositional deviation from the desired stoichiometry of the PMN–PT films. The epitaxial PMN–PT films deposited using the single-crystal target showed a higher dielectric constant (1926) and remnant polarization (11.9 μC/cm^2) than the films deposited using a ceramic target. All the observations suggest the superiority of a single-crystal target over the ceramic target for the growth of epitaxial PMN–PT films with high crystallinity and good ferroelectric properties.

Acknowledgements

This work was funded by the Ministry of the Economy, Science and Technology (MEST) (No. 2011-0000359). This work is also the Outcome of a Manpower Development Program for Energy & Resources supported by the Ministry of Knowledge and Economy (MKE) and was supported by the Brain Korea 21 Project in 2006.

References

[1] C.H. Ahn, K.M. Rabe, J.-M. Triscone, Science 303 (2004) 488–491.
[2] J. Jiang, H.H. Hwang, W.J. Lee, S.G. Yoon, Sens. Actuators B: Chem. (2011), doi:10.1016/j.snb.2011.01.061.
[3] J. Wu, J. Wang, J. Alloys Compd. 507 (2010) L4–L7.
[4] J. Jiang, S.G. Yoon, J. Alloys Compd. 509 (2011) 3065–3069.
[5] M. Feng, W. Wang, H. Ke, J.C. Rao, Y. Zhou, J. Alloys Compd. 495 (2010) 154–157.
[6] B.T. Liu, C.S. Cheng, F. Li, D.Q. Wu, X.H. Li, Q.X. Zhao, Z. Yan, X.Y. Zhang, J. Alloys Compd. 440 (2007) 276–280.
[7] L. Krishna, M. Sunder, P.D. Moran, J. Electron. Mater. 39 (2010) 132–137.
[8] A.R. Chaudhuri, S.B. Krupanidhi, P. Mandal, A. Sundaresan, J. Appl. Phys. 106 (2009) 054103–54107.
[9] K.G. Webber, R. Zuo, C.S. Lynch, Acta Mater. 56 (2008) 1219–1227.
[10] Y. Li, K. Tanabe, J. Appl. Phys. 83 (1998) 7744–7752.
[11] K. Shinozaki, S. Hayashi, N. Wakiya, T. Kiguchi, J. Tanaka, N. Ishizawa, K. Sato, M. Kondo, K. Kurihara, IEEE T. Ultrason. Ferr. 55 (2008) 1023–1028.
[12] F. Wu, X. Li, W. Yu, X. Gao, J. Cryst. Growth 310 (2008) 575–578.
[13] M. Detalle, G. Wang, D. Remiens, P. Ruterana, P. Roussel, B. Dkhil, J. Cryst. Growth 305 (2007) 137–143.
[14] N. Scarisoreanu, F. Craciun, G. Dinescu, P. Verardi, M. Dinescu, Thin Solid Films 453–454 (2004) 399–405.
[15] B. Noheda, D.E. Cox, G. Shirane, Phys. Rev. B 66 (2002) 054104–54110.
[16] S. Choudhury, Y.L. Li, L.Q. Chen, Q.X. Jia, Appl. Phys. Lett. 92 (2008) 142907–142913.
[17] H.N. Lee, S.M. Nakhmanson, M.F. Chisholm, H.M. Christen, K.M. Rabe, D. Vanderbilt, Phys. Rev. Lett. 98 (2007) 217602–217604.
[18] M. Alguero, M. Stewart, M.G. Cain, P. Ramos, J. Ricote, M.L. Calzada, J. Phys. D: Appl. Phys. 43 (2010) 205401–205406.